Title
Experimental Investigation of Postearthquake Vertical Load-Carrying Capacity of Scoured Reinforced Concrete Pile Group Bridge Foundations

Journal
Journal of Bridge Engineering, 26(12)

ISSN
1084-0702

Authors
Zhou, Lianxu
Barbato, Michele
Ye, Aijun

Publication Date
2021-12-01

DOI
10.1061/(asce)be.1943-5592.0001799

Peer reviewed

Experimental Investigation of Post-Earthquake Vertical Load-Carrying Capacity of Scoured Reinforced Concrete Pile Group Bridge Foundations

Lianxu Zhou[1], Michele Barbato[2], Aijun Ye[3]

[1]Ph.D. candidate, State Key Laboratory of Disaster Reduction in Civil Engineering, Tongji University, Shanghai 200092, China. Email: csuzlx@tongji.edu.cn

[2]Professor, M.ASCE, Department of Civil and Environmental Engineering, University of California, Davis, CA. Email: mbarbato@ucdavis.edu

[3]Professor, State Key Laboratory of Disaster Reduction in Civil Engineering, Tongji University, Shanghai 200092, China (Corresponding author). Email: yeaijun@tongji.edu.cn

Abstract: Scouring of pile group foundations is a common phenomenon for cross-river bridges and can produce significant damage in earthquake-prone regions. This study experimentally investigated the seismic failure mechanism and post-earthquake vertical load-carrying capacity of scoured pile group foundations. Three identical 2×3 reinforced concrete (RC) pile group specimens were embedded in homogeneous medium density sand with an overall scour depth equal to five times the diameter of a single pile, and then were subjected to lateral cyclic loads applied to the pile cap in order to produce a predetermined damage state in the piles. Pushover in the vertical-downward direction (pushdown) was finally applied on these damaged specimens exhibiting a permanent lateral displacement to evaluate their residual load-carrying capacities. Experimental results show that the leading pile was more prone to seismic damage, as both the first aboveground and first belowground plastic hinges originally occurred on it. The embedded depth of potential plastic hinges in leading, middle, and trailing piles gradually increased. In addition, the extension of pile damage had a significant influence on the residual vertical load-carrying capacity and the corresponding vertical failure mode of the pile group. Reductions of 10.4%, 47.5%, and 73.8% in the vertical load-carrying capacity of these scoured pile group specimens were recorded when they previously suffered a displacement ductility of 1.75, 3.5, and 5.0, respectively. Based on the experimental results, a linear degradation formula on the normalized post-earthquake vertical load-carrying capacity of pile groups with respect to the displacement ductility was developed. The experimental results presented in this paper could be used to validate the ductility capacity and residual vertical load-carrying capacity of pile groups numerically evaluated by using three-

dimensional nonlinear finite-element models. This research represents also a first step toward the development of a rapid post-earthquake assessment approach for bridges with pile group foundations.

Keywords: pile group foundation; bridge scour; soil-pile interaction; seismic damage; post-earthquake residual strength; ductility capacity; pushdown test.

Introduction

Reinforced concrete (RC) pile group foundations are extensively utilized in bridge engineering as they exhibit high resistance to gravity loads and are easy to build. In a pile group foundation, all pile heads are connected together by a cap. Many current specifications stipulate that pile group foundations should be designed to behave elastically under design-level earthquakes based on the capacity design philosophy (Mander et al. 1998). However, pile damage is still unavoidable when the pile-bridge system is subjected to unexpectedly large earthquakes (Kawashima et al. 2009; Wei et al. 2008). In addition, scour is a main hazard for cross-river bridges (Wardhana and Hadipriono 2003). Due to the riverbed scour (i.e., water-induced erosion), soil around the pile groups is eroded, resulting in the exposure of the pile shafts near the cap (Shang et al. 2018; Wang et al. 2019c). The exposure of pile shafts reduce the lateral and vertical load capacity of a pile group. In addition, the earthquake-induced damage tends to be transferred from column to piles as the pile-supported bridges are subject to scour (Wang et al. 2015, 2019d, 2014). Therefore, the scoured pile groups are generally subjected to a higher risk of earthquake-induced damage in earthquake-prone regions than their counterparts without scour, particularly for older pile-supported bridges built prior to the implementation of the capacity design approach. Pile damage could result in a permanent displacement of the pile group and the superstructure, and reduce the vertical load-carrying capacity of the foundations (Bhattacharya et al. 2008; Lin and Liao 1999; Wang et al. 2019b). Presently, experience-based post-earthquake inspections and engineering judgement represent the main tools to estimate the remaining traffic capacity of a damaged bridge (O'Connor and Alampalli 2010). However, the unobservable pile damage located below the soil surface makes it difficult and time-consuming to decide whether to reopen these damaged bridges for emergency traffic after an earthquake. Hence, it is essential to quantitatively investigate post-earthquake load-carrying capacity of pile foundations under different damage levels and understand their potential seismic failure mechanisms.

This study employs the quasi-static test method to investigate experimentally the behavior of damaged scoured pile groups. This experimental method has been used extensively to investigate the ductile behavior and the load-carrying capacity of structural specimens due to its simplicity and cost effectiveness (Wang et al. 2019a). This testing technique was used to investigate the ductility capacity of single piles (Banerjee et al. 1987; Park and Falconer 1983), and extended pile shafts (Chai and Hutchinson 2002). Lemnitzer et al. (2010) and Rollins et al. (2003, 2006) carried out a series of quasi-static tests on pile groups, which were mainly focused on assessing the pile group effect. More recently, Wang et al. (2016) and Liu et al. (2020) experimentally investigated the seismic failure mechanism of 2×2 and 2×3 pile group foundations considering the impact of pile shaft exposure. However, their test specimens consisted of piles with a square section, whereas circular piles are more common in real-world applications. Research on the post-earthquake load-carrying capacity of structural components has been relatively limited. Tasai (2000) investigated the residual axial capacity of RC columns during shear degradation. Elwood and Moehle (2005) developed an axial capacity model for shear-damaged columns. Terzic and Stojadinovic (2015a, 2015b; 2010) experimentally investigated the post-earthquake residual load-carrying capacity of bridge columns under different ductility demand conditions using a test technique named as “push-under”. They reported an approximate 20% reduction in vertical load-carrying capacity of columns after undergoing a maximum displacement ductility demand of 4.5 and being brought back to a zero residual displacement. However, since the damaged column specimens were re-centered before performing the push-under test, the impact of permanent displacement on the residual load-carrying capacity of the columns was not taken into account in their experiments. To the best of the authors’ knowledge, the residual load-carrying capacity of pile group foundations under different lateral damage levels (corresponding to different permanent deformations) has not been yet fully investigated in the literature, albeit it represents an indispensable information to properly model a pile-supported bridge system after it is affected by a major earthquake.

This study aims to experimentally investigate the residual vertical load-carrying capacity of scoured RC pile group foundations subjected to different damage levels. To this end, three 2×3 pile group foundation specimens (i.e., six circular piles connected by a cap) were constructed and tested in the indoor structural laboratory at Tongji University, Shanghai, China. Each specimen was laterally loaded along its strong axis by imposing a series of cyclic displacements until a predetermined damage state (or ductility level) was reached. A pushdown test was then performed on these damaged specimens exhibiting a permanent lateral displacement. The seismic failure mechanism and the ductility capacity of these pile group specimens were obtained. Finally, a quantitative evaluation for the post-earthquake load-carrying capacity of pile groups under different ductility demand conditions was performed.

Novelty and Relevance

This study represents the first experimental investigation of the post-earthquake vertical load-carrying capacity of scoured RC pile group foundations using quasi-static tests. The experimental data presented in this paper are extremely valuable for modeling calibration and validation for future numerical investigations of soil-pile interaction and post-earthquake load-carrying capacity evaluation of pile group foundations. This research represents a key step toward the development of a rapid post-earthquake assessment approach for bridges with pile group foundations.

Quasi-static Test Setup

Specimen configurations and instrumentations

A 2×3 pile group was designed based on the capacity of lateral and vertical actuators, as well as on the indoor laboratory space capabilities at Tongji University. Three identical specimens were built for the planned test. Figure 1 illustrates an overview of the pile group specimens, whereas Figure 2 presents some photographs of the test layout for one of the physical specimens. Each specimen consisted of six circular piles with a length H = 4.3 m and a diameter D = 0.12 m. These piles were placed in three rows along the lateral loading direction (i.e., east-west direction), and their pile heads were connected together by a cap with dimensions of 1.5 × 1.0 × 0.6 m, where 1.5 m is the length in the loading direction, 1.0 m is the width perpendicular to the loading direction, and 0.6 is the thickness in the vertical direction. The center-to-center pile spacing both in parallel and perpendicular to the loading direction was 3D. In order to model the scour effect, a portion of length 3.7 m (30.83D) out of the total length of each pile was embedded in homogeneous sand with a relative density D_r = 51% ~ 58%, which represented a 0.6 m (5D) overall scour depth. To minimize soil container boundary effects, the specimen was positioned in the central area of the container with an inside dimension of 3.1 (length) × 1.5 (width) × 4.2 m (height). The distances between the outer piles and the soil container walls in east-west and north-south directions were 9.42D and 4.25D, respectively (see Figure 1b). As shown in Figures 1a and 2b, the lateral load was provided by a servo-controlled hydraulic actuator (referred to as actuator #1) with a 50-cm-stroke and 500-kN-capacity. One end of this actuator was mounted on the reaction wall and the opposite end was connected to the center of the vertical surface of the pile group cap through bolts. To minimize the influence of the self-weight of actuator #1 on the cap rotations, the front end of actuator #1 was hung from a cantilever (mounted on the reaction wall) through two springs. Vertical loads were provided by a 200-cm-stroke/1600-kN-capacity servo-controlled hydraulic actuator (referred to as actuator #2), whose upper end was suspended from a bidirectional sliding rail that was installed on a 3000-kN-capacity counterforce frame, as shown in Figure 2a. Therefore, actuator #2 remained vertical during all loading phases since its upper end synchronously moved with the specimen in the horizontal direction.

Figures 1 and 2 also display the instrumentations used in the test. Three 1000-mm-length linear variable displacement transducers (LVDT) were installed on the cap to trace its lateral displacements along the loading direction. Among the three LVDTs, the middle one was used to control the lateral displacement loading, whereas the other two were used to indirectly trace the cap rotations through geometric transformation of the data measured by them. The cap rotation was also directly measured by one inclinometer attached on the top of the cap, as shown in Figure 1b and Figure 2e. The strain of longitudinal rebars at the eastern and western edges of the pile sections were monitored by 16 pairs of strain gauges, and their distribution along the pile shaft are shown in Figure 1c. These strain gauges were also used to calculate the cross-section cruvature during the tests. Since strain gauges were expected to malfunction for highly nonlinear behavior of the rebars they were attached to, linear potentiometers were also pairwise placed along the aboveground piles in the regions of length 3D below the pile heads to trace the average section curvatures. Detailed transformation procedures to calculate the section curvature from the displacement measured by linear potentiometers can be found in the literature (Zhou et al. 2019). Due to the limited number of data acquisition channels and sensors, both strain gauges and linear potentiometers were placed only on three of the six piles, which are highlighted in gray color in Figure 1b. In addition, four laser sensors (identified by red stars in Figure 1b) were fixed on an external steel pipe frame (Figures 2a and 2d) and placed over the cap top to measure its vertical displacement. The mean values of the cap displacements in the vertical direction measured by the four laser sensors in pushdown phase are considered representative of the vertical displacement of the specimen, thus eliminating the influence of the cap rotations.

Pile reinforcements and section moment-curvature analysis

As shown in Figures 1c and 1d, six 6-mm-diameter longitudinal rebars were annularly assembled in the pile sections and provided a longitudinal steel reinforcement ratio of 1.5%. All longitudinal steel reinforcement bars in each pile were extended 58 cm into the cap to ensure a reliable pile-cap connection. The core concrete of the piles were spirally confined by 3.5-mm-diameter galvanized-iron-wires (GIWs) spaced at 35 mm, leading to a transverse steel reinforcement ratio of 1.215%. The thickness of the concrete cover was 13 mm, which was measured from the outside face of the GIWs to the pile surface. Six plain concrete cylinders with a height of 300 mm and a diameter of 150 mm, cast on the same day when the pile group specimens were fabricated, were tested to determine the elastic modulus and peak strength of the concrete by compression tests (i.e., three specimens for the former and other three specimens for the latter). Three rebars and three GIW specimens were also tested to determine their mechanical parameters via tensile tests. These tests were performed on the sixth day before the commencement of the quasi-static test. Table 1 lists the average values and the coefficients of variation (provided as percentage in parentheses) of the measured mechanical parameters for the concrete and steel reinforcements employed in the specimen fabrication.

A moment-curvature analysis for the pile section was performed by using the OpenSees software framework (McKenna 2011). The pile section was modeled by using a zero-length element with fiber discretization of the cross-section. Different constitutive models were assigned to fibers corresponding to concrete cover (unconfined concrete), concrete core (GIW-confined concrete), and longitudinal steel rebars. In particular, the concrete fibers were modeled by using the uniaxial constitutive model denoted in OpenSees as *Concrete01*, which corresponds to the Kent-Scott-Park model with zero strength in tension (Scott et al. 1982). This model can better represent the post-peak degrading slope and stress-strain behavior of GIW-confined concrete (Terzic and Stojadinovic 2015a). The strains corresponding to peak compressive strength and crushing strength of the unconfined concrete were taken as 0.002 and 0.006, respectively (Barbato et al. 2010), as they were not measured in the testing of the concrete cylindrical specimens. The peak strength of the confined concrete was taken as 29.05 MPa, which was calculated by using the formula recommended by Scott et al. (1982). The strain at peak strength and the ultimate strain of the confined concrete were taken equal to 0.0037 and 0.021, respectively, based on the experimental data of short columns presented in last section. The residual strengths of both confined and unconfined concrete were taken as 20% of their corresponding peak strengths. The longitudinal rebars were modeled by using the uniaxial constitutive model denoted in OpenSees as *Steel02*, which corresponds to the Menegotto-Pinto model with isotropic strain hardening (Filippou et al. 1983). A quasi-static analysis was performed by using a displacement-controlled pattern, with a rotation increment equal to 5.0×10^{-3} rad. The NewtonLineSearch algorithm with a tolerance of 0.8 in OpenSees was used to solve the resulting non-linear equations (Mazzoni et al. 2006).

Figure 3 presents the moment-curvature results for the pile section subject to an axial load ratio of 5%, which corresponds to the axial load ratio of the test piles under dead loads only. The axial load ratio is defined here as the ratio between the applied axial load and axial strength of the pile obtained as the product of the unconfined concrete peak strength and the pile cross-section gross, consistently with the definition used in the literature (Lam et al. 2003). Wang et al. (2016) and Liu et al. (2020) reported that the yielding curvature of a pile section is not sensitive to axial load variations. By contrast, they found that the ultimate curvature is highly dependent on axial load variations. This study employs the yielding curvature of a pile section to identify the yielding sequence of piles. Therefore, although the axial loads applied on piles generally vary when a pile group is subjected to lateral loads, the axial force variation was not taken into account in the moment-curvature analysis of the pile section, because its effect on the pile yielding curvature is negligible. The analysis results indicate that the ultimate curvature of the pile section is 0.838 rad/m and corresponds to crushing of the core concrete, which occurs before the rupture of the longitudinal steel rebar. Based on the computed moment-curvature curve, the equivalent yielding curvature of the pile cross-section was estimated as 0.045rad/m. This curvature was obtained from the idealized bilinear moment-curvature curve (identified by dashed lines in Figure 3), and corresponded to the curvature of the intersection between the elastic line (with slope equal to the secant stiffness between the origin and the point of first yielding on the numerical moment-curvature curve) and the horizontal line corresponding to fully-plasticized cross-section. Hereinafter, the equivalent yielding curvature is used to determine if a cross-section has reached plasticization.

Soil properties and placement

Dry yellow silicon sand from Shanghai, China, was used as the surrounding soil for the test piles. The particle size distribution for this sand is shown in Figure 4. The average grain size of the sand, D_{50}, was 0.293 mm, and the uniformity coefficient C_u (which is defined as the ratio of the grain size corresponding to 60% and 10% passing materials, D_{60}/D_{10}) is 2.5. The measured maximum and minimum dry bulk densities were 17.23 kN/m^3 and 14.01 kN/m^3, respectively. The moisture content of the test sand was 0.16%.

Before the placement of the sand, the precast pile group specimen was placed first in the soil container and supported vertically on one 4-cm-thickness square steel plate mounted at the bottom of the container. It is pointed out that this configuration of the experiment was representative of a pile group with end bearing on rock/stiff substrata. To ensure a uniform compaction of the soil, the 3.7-m-depth sand was placed sequentially in thirteen layers (i.e., the first twelve layers with an approximately same thickness of 30 cm and the last layer with a thickness of 10 cm). Each sand layer was artificially compacted using wooden hammers. Note that slight differences between the actual and target compaction thickness for each soil layer were inevitable. This thickness variability resulted in a slight variation of the relative density of sand, which was contained between 51% and 58%.

Test procedure

Figure 5 presents the test loading protocol. A three-phase test loading protocol, inspired by the test loading procedure used in Terzic and Stojadinovic (2015a), was adopted to investigate the residual load-carrying capacity of the three pile group specimens at different damage states, as well as to identify their failure mechanism. The protocol used in this study included lateral loading (first and second phases of the test) followed by the pushdown test (third and last phase of the test). In the first phase, lateral cyclic displacements following the predesigned loading protocol at a constant rate of 0.5 mm/s were imposed on the pile cap to produce the target damage levels, as listed in Table 2 for the three specimens. In particular, the lateral loading protocols for specimens #1, #2, and #3 were selected so to reach the first-yielding of the belowground pile shafts, the onset of the lateral strength degradation (i.e., by loading the specimen up to its peak lateral strength), and a 15% degradation of the lateral strength, respectively. The maximum lateral displacement levels applied to specimens #1, #2, and #3 were 35 mm, 70 mm, and 100 mm, respectively. The values of the lateral displacement levels corresponding to the selected damage states of interest were based on the data obtained from testing specimen #3 before the other two specimens, i.e., by measuring the displacements at which first-yielding of the belowground pile shaft and onset of lateral strength degradation took place, and by interrupting the test as soon as a 15% degradation of the lateral strength was observed. All specimens were returned to a zero-displacement state of their cap at the end of the first loading phase. The second loading phase was used to simulate the residual deformation state of pile group foundations after an earthquake. Each specimen was loaded again to the maximum displacement level reached in the first loading phase, and then unloaded to a zero-lateral force state (i.e., the so-called residual displacement state). After that, the horizontal actuator (actuator #1) was carefully separated from the specimen after unscrewing the nuts from the cap-actuator connections. In the first and second lateral loading phases, the initial axial force on the piles was set equal to an axial load ratio of 5% and was provided by the combination of the load applied by actuator #2 (i.e., 62.0 kN) and the cap weight (i.e., 23.4 kN). In the third and last loading phase, a pushdown test on the damaged specimens at their residual deformation state was performed through actuator #2 using a displacement-controlled monotonic loading with a constant rate of 1.0 mm/min.

Verification of soil container boundary conditions

In order to ensure the validity of the experimental results, the boundary conditions provided by the soil container need to correspond to a negligible lateral soil pressure. Two soil pressure sensors were attached on the west side (i.e., along the loading direction) and the south side (i.e., perpendicularly to the loading direction) of the soil container walls at the depth of 4D and 2D, respectively. An additional soil pressure sensor was installed on the leading pile along the loading direction at the depth of 4D. Figure 6 compares the peak soil pressure measured on the leading pile and the container walls at different displacement levels. It is observed that the boundary effects in this test can be neglected, as the peak lateral soil pressure measured on the west side and the south side of the container wall were equal to 0.017 MPa and 0.003 MPa, respectively, which were negligible when compared to the peak soil pressure measured on the leading pile (i.e., 0.288 MPa). These results also indicate that the soil domain dimensions of 9.42 D and 4.25 D along and perpendicular to the loading direction, respectively, were sufficient to minimize the boundary effects in the soil-pile interaction tests performed for the present study.

Seismic Failure Mechanism and Ductility Capacity

Pile group hysteretic behavior

The hysteretic lateral force versus displacement responses for the three specimens are shown in Figure 7a, and the response envelope profiles of each specimen are plotted in Figure 7b. Because displacement-force responses for each specimen under three cyclic loadings with the same displacement amplitude were almost identical, only the responses corresponding to the second cycle of each displacement amplitude are presented herein for the sake of clarity. It is observed that the responses of the three specimens almost coincide for the same displacement levels, and that the lateral forces at maximum displacement of each specimen in both push and pull directions are very close (i.e., +28.3

kN and -31.3 kN for specimen #1, +28.3 kN and -31.5 kN for specimen #2, and +27.5 kN and -27.4 kN for specimen #3). The small variability of these results shows that the mechanical properties and the sand condition are fairly consistent among all specimens. In addition, the wide hysteretic loops observed in these tests indicate a high ductility and a stable response for the pile group.

Pile curvature distribution and plastic hinge developments

Figure 8 presents the section curvature distributions along the pile shafts at the peak displacements for different loading cycles (i.e., 10, 20, 30, 40, and 50 mm) in the push and pull directions, respectively. Note that a few strain gauges in the potential plastic hinge region of the piles malfunctioned after yielding of the longitudinal reinforcement, causing the loss of information on the corresponding pile section curvatures. In particular, the loss of belowground strain gauges started between displacement levels of 40 and 50 mm in a few locations (characterized by large curvatures) on the leading and trailing piles below soil surface, and then expanded rapidly to other locations for larger displacement levels. Therefore, Figure 8 presents the curvature distributions along the pile shafts only up to a displacement level of 50 mm. For the 50 mm displacement level, the locations where the strain gauges malfunctioned are marked by the symbol “×”, and report the last curvature value recorded before the loss of the corresponding strain gauge. As soon as the strain gauges at pile heads were disabled, the pile head curvature was calculated from the data measured by linear potentiometers. These values are identified by circles in Figure 8. It is pointed out that the outer piles in the pile group alternately played the role of leading and trailing piles under cyclic loads, i.e., piles 1 and 3 in each specimen acted as the leading and trailing piles in the push direction, respectively; whereas they correspondingly converted to trailing pile and leading pile in pull direction. As shown in Figure 8, a similar curvature distribution of the pile shaft was recorded in correspondence of the same lateral displacement level when pile 1 and pile 3 acted as the leading (or trailing) piles, respectively.

The equivalent yielding curvature of the pile section, which was found to be equal to 0.045 rad/m from the moment-curvature analysis, is also represented in Figure 8 as vertical dashed lines. This quantity is used as the basis to identify whether the pile section yields at a given displacement level. It is observed that the lateral loading phase of the test produced two plastic hinges on each pile in the scoured pile group: the first hinge was located at the pile head, whereas the second hinge occurred on the pile shaft below the ground surface, and the contraflexure point (indicated by filled markers) was located near the ground surface, as shown in Figure 8. This phenomenon also implies that the three piles standing in a line along the lateral loading direction formed a frame-like structure. By comparing the curvature envelopes of different piles at the same displacement level, it is observed that the curvature of each pile section at the same elevation decreased from the leading to the middle pile and from the middle to the trailing pile. This result implies that the leading pile carried a larger proportion of the lateral loads on the pile group foundations than the middle and trailing piles, due to the pile group effect. This phenomenon was also reported by Rollins et al. (2005). In addition, the embedded depth of the maximum curvature for a belowground pile section gradually increased when going from the leading (i.e., between -5D and -6D), to the middle (i.e., between -7D and -8D), to the trailing (i.e., between -9D and -10D) piles. Within the same pile, the embedded depth of the belowground section with maximum curvature tended to decrease with the increase of the displacement levels. It is also observed that the section curvature at the pile head was larger than that of all other sections along the pile shaft under any displacement level. These findings indicate that the leading pile, and especially its pile head, was more prone to seismic damage than the other piles, as both the first aboveground and first belowground plastic hinges originally occurred on it. This conclusion is also consistent with the experimental results reported by Liu et al. (2020).

In the test performed for this study, the pile heads of the leading piles (i.e., piles 1 and 3) were the first locations to reach yielding at a displacement level of approximately 20 mm. The first belowground plastic hinges also occurred on the leading piles, as the lateral displacement increased to 35 mm. After that, the second belowground plastic hinge was formed on the middle pile at a displacement level of approximately 50 mm. Table 3 lists the measured pile head curvatures at displacement levels of 35 mm, 70 mm, and 100 mm. Also for these results, in general, it is observed that the curvature of the pile head gradually decreased from leading, to middle, to trailing piles for a given displacement level. At the displacement of 100 mm, the pile head of the leading pile reached its ultimate curvature, which corresponds to the condition of core concrete crushing.

Displacement ductility of pile group specimens

The local section curvature ductility cannot fully describe the global damage state of a pile group foundation because multiple plastic hinges can occur on the different piles, as also shown in the present study. Therefore, Blanco et al (2019) proposed the displacement ductility (μ_D) as a global damage index for a pile group, which is defined as:

$$\mu_D = \frac{\Delta}{\Delta_y} \tag{1}$$

where Δ_y is the horizontal displacement of the cap center corresponding to the first section yielding of any pile in the pile group, and Δ represents the cap horizontal displacement corresponding to a specific damage state. In this study, a section yielding is identified when the curvature of a section reaches the equivalent yielding curvature as determined by the cross-sectional moment-curvature analysis reported in Figure 3. In this test, the yield displacements were measured for the three specimens as 20.0 mm, 19.8 mm, and 20.1 mm, respectively. Given the small variations among the two specimens (i.e., with differences smaller than 1 mm), the average value Δ_y = 20 mm was used to calculate the experimental displacement ductility of the three specimens. Table 4 lists the measured displacement ductility of the specimens at different damage states, as well as the maximum curvature ductility of the first aboveground plastic hinge in the leading pile. It is observed that the pile group specimens exhibited a considerable displacement and curvature ductility capacity.

Pile-cap rotations and pile head crack developments

Figure 9 presents the measured peak and residual cap rotation angles of specimen #3 at different lateral displacement levels. The residual cap rotation is defined here as the tilt angle of the pile group at the zero-lateral force state. To check the measurement accuracy of the cap rotation, the cap rotations measured by using the inclinometer were compared with the results calculated from the LVDT data via geometric transformation. In general, very similar cap rotation values were obtained by these two measurement methods. The recorded data indicate an approximately symmetrical cap rotation-peak displacement relation in the push and pull directions.

Two fitting formulas for the peak and residual cap rotations with respect to the displacement ductility are proposed as follows:

$$\theta_P = \frac{7}{5000}\mu_D \quad 0 \le \mu_D \le 5 \tag{2}$$

$$\theta_R = \begin{cases} 0 & 0 \le \mu_D < 2 \\ \frac{1}{5000}(\mu_D^2 - 2\mu_D) & 2 \le \mu_D \le 5 \end{cases} \tag{3}$$

where θ_P and θ_R denote the peak and residual cap rotations, respectively. These equations could be used to predict the cap peak and residual rotation for pile groups exhibiting a specified ductility. However, these equations should also be validated with additional experimental data, including at a minimum different configurations for the pile groups, different levels of scour, and different soil types and relative densities.

The progression of cracking in the aboveground portion of the pile shafts was also investigated through direct observation and measurements. Overall, the cracks progressed in a similar fashion in the three specimens. Initially, three horizontal hairline cracks with an average spacing of 6 cm (0.5D) occurred in the regions of length 2D below the pile head of the leading piles at the displacement level of 10 mm (μ_D = 0.5). At this displacement level, two similar cracks occurred also on the middle pile heads. Subsequent loadings produced additional cracks on piles, which were horizontally distributed in the regions of length 3D below the pile heads with a spacing of 3-6 cm. After the lateral displacement exceeded 40 mm (μ_D = 2.0), almost no new horizontal cracks occurred in the aboveground portion of the piles. In addition, no diagonal cracks were observed during the lateral loading phase.

A clip gauge was employed to record the variation of the main crack of a leading pile within the displacement ductility range between 0.75 and 1.75. The feasibility of using clip gauges to record the crack progression was confirmed by Guan et al. (2017). The clip gauge was located at approximately 8 cm below the pile head on the leading pile. Due to an insufficient installation space for the clip gauge, it was not possible to measure the progression of another crack observed near the pile head, even though this crack seemed wider than the measured one under visual inspection. Figure 10a shows the variation of the crack width with respect to the applied lateral force for different lateral displacement levels. Since the lateral force-crack width curves for 15 mm and 20 mm of lateral displacement are very similar, the former is not shown for the sake of clarity. It is observed that, after opening during the loading phases, the crack gradually reclosed during the unloading phases. Figure 10b compares the measured crack widths at the maximum loading value, at the residual displacement state (i.e., zero-lateral load condition), and at the zero-cap displacement state. For clarity, the crack widths at these different states are marked on the curve corresponding to 35 mm of lateral displacement in Figure 10(a). It is observed that the zero-lateral force crack width was always larger than the corresponding zero-cap displacement crack width at the same displacement level. This result was expected because the zero-lateral force conditions correspond to residual deformations, which are removed when considering the zero-cap displacement conditions. This finding suggests that using the crack width corresponding to zero-cap displacement state can significantly underestimate the residual-crack damage, which is consistent with the findings reported by Guan et al. (2017).

Moreover, the residual cracks started forming as soon as the pile group reached yielding (i.e., for displacement ductility approximately equal to 1), as shown in Figure 10b. Similar observations were also made by Yeh et al. (2002). In the present test, the measured crack widths before the cross-section yielding of the belowground pile shaft were 0.61 mm at the maximum value, and 0.28 mm at the zero-lateral force state (i.e., the residual crack width was equal to 0.28 mm). Therefore, only hairline residual cracks (i.e., barely visible to the naked eye) occurred on the piles before the formation of any belowground plastic hinge. Under these conditions, retrofitting of the piles would not be required. In fact, according to Hose and Seible (1999) and Guan et al. (2017), residual cracks with a width smaller than 0.3 mm are barely visible, correspond to a fully operational condition for a RC structure, and do not require any repair.

Summary of observed damage and residual displacements of specimens

Table 5 summarizes the global performance and local damage descriptions for the three pile group specimens at different damage states. Figure 11 shows some pictures of the aboveground portions of the pile group at the zero-lateral force state (or residual displacement state) corresponding to each damage state. In this study, only hairline residual cracks were detected in the pile head regions when specimen #1 reached the belowground cross-section yielding for the pile shafts (corresponding to μ_D = 1.75). Limited cover concrete spalling was observed on the pile heads of the leading and middle piles when specimen #2 underwent the onset of lateral strength degradation (corresponding to μ_D = 3.5). Finally, extensive cover concrete spalling was observed on the pile heads of the leading and middle piles when specimen #3 experienced a 15% degradation of the lateral strength (corresponding to μ_D = 5.0). In correspondence to this damage state, some local core concrete crushing was also observed on the leading piles. In addition, the pile damage caused a permanent lateral displacement on the pile cap, which was equal to 14 mm, 40 mm, and 68 mm for specimens #1, #2, and #3, respectively, corresponding to residual drift ratios of 1.16%, 3.33%, 5.66%, respectively. The residual drift ratio herein is defined as the ratio between the permanent cap displacement in the horizontal direction and the distance between the cap top surface and the soil surface (i.e., 1.2 m or 10D). It is observed that the residual cap rotations were always very small, with a maximum value of 3.9×10^{-3} rad for specimen #3. Since the pushdown test needed to be performed on these laterally-damaged pile groups, the belowground pile conditions were not inspected at the end of the lateral loading phases and no direct observation of the belowground damage states is available.

An increasing gap between the leading pile and its surrounding soil was observed for increasing displacement levels. This phenomenon was caused by the lateral compaction of the sand in front of the leading piles. As shown in Figure 11, this compaction resulted in a clearly visible localized hole near and in front of the leading piles, while a slight global sand settlement was also observed in the test around the middle piles. For example, for the specimen #3, the sand hole at east side had a depth of approximately 18 cm and a width of approximately 80 cm, and the global sand settlement around the middle piles was approximately 7.2 cm (i.e., 0.6D). A similar phenomenon was also reported by Wang et al. (2016). Note that since the residual deformation of the pile group at each damage state was towards the push direction (or west side), the final local hole at the east side was wider and deeper than that at the west side. By contrast, the width of the residual cracks on the aboveground portion of the pile shafts at the east side was smaller than that at the west side. As shown in Figure 11, the sand hole at the east side gradually became wider and deeper for the three damage states.

Post-earthquake Load-carrying Capacity of Pile Group at Different Damage States

Vertical load-carrying capacity estimation for the undamaged pile group specimen

The vertical load-carrying capacity of the undamaged pile group specimens (referred to as initial vertical load-carrying capacity hereinafter) was estimated in order to provide a basis for comparison of the test results on the damaged pile group specimens. This estimate was performed indirectly because of the limited capacity of actuator #2 (i.e., 1600 kN), which was deemed insufficient to reach the expected peak vertical load-carrying capacity of the 2×3 pile group considered in this study. In particular, the initial vertical load-carrying capacity of the pile group specimen was estimated as six times the strength of a single pile. Due to the constraints imposed by the surrounding soil and the cap, the piles in the studied pile group specimen formed a frame-like structure, and the boundary condition of the pile at the soil surface is closer to a hinged end, as indicated by the position of the contraflexure point reported in the figure 8. When the undamaged pile group is subject to vertical load only, the horizontal displacement of each pile could be restrained by whole pile group. Therefore, each pile under axial loads could be analyzed as an equivalent column with an approximately fixed end at the cap bottom and hinged end at the soil surface. Due to the loading condition corresponding to vertical load only for the undamaged pile group, each pile in the pile group specimen was equivalent to an axially loaded column with a length equal to 60 cm (i.e., 5D) and an effective length coefficient smaller than or equal to 1. Because of the small length-to-diameter ratio (corresponding to a slenderness smaller than or equal to 20), each pile was considered as a short column. Thus, the strength of the individual pile was estimated both experimentally through axial compression tests on three short columns, and numerically through a finite-element sectional analysis. The length of the short column's physical specimens was selected equal to 3D based on the capabilities of the available experimental testing equipment.

The three short columns had a length equal to 36 cm, and a diameter equal to 12 cm. These columns had the same transversal and longitudinal steel reinforcements used for the piles in the pile group specimens, and were fabricated on the same day of and with the same materials used for the pile group specimens. The short columns were subjected to a displacement-controlled axial loading with a displacement of 0.216 mm/minute (corresponding to a strain rate of 1×10^{-5} s^{-1}). The experimental axial force-axial strain response of the three columns is shown in Figure 12. The peak strengths of the three columns were 265 kN, 291 kN, and 283 kN, respectively, corresponding to an average peak strength is 280 kN. A numerical analysis of the axial behavior of the same pile section was also performed in OpenSees. The modeling details, analysis type, and material parameters used to describe the confined and unconfined concrete and longitudinal steel rebars were identical to those used in the moment-curvature analysis of the pile section. To account for accidental eccentricity, an eccentricity-to-diameter ratio of 0.05 (corresponding to an axial load eccentricity equal to 6.0 mm) was assumed in the axial section analysis for the pile section, based on the recommendation of ACI 318 for columns with spirals (ACI 2014). The numerical axial force-axial strain response for the pile section is also shown in Figure 12. The numerical analysis provided a peak strength for the section equal to 286 kN, which is consistent with the experimental results obtained from the short columns. Based on these results, the initial vertical load-carrying capacity of the 2×3 pile group specimen was assumed equal to 1680 kN, i.e., 6 times the average peak strength obtained from the experimental results of the axial compression tests performed on the short columns.

Post-earthquake vertical load-carrying capacity and failure mode

The residual vertical load-carrying capacity of the laterally-damaged pile group specimens (i.e., with the permanent lateral displacement induced by the cyclic loading phases) were evaluated via a pushdown test. Figure 13 plots the applied vertical load and the cap lateral displacement versus the vertical displacement increment for the three pile group specimens. The initial vertical load of 62 kN corresponding to zero vertical displacement increment represents the dead load applied to the pile group. Figure 14 shows some pictures of the physical specimens after completion of the test and removal of the surrounding soil.

The residual vertical load-carrying capacity of specimen #1 was 1505 kN, which corresponded to 89.6% of the initial vertical load-carrying capacity of the undamaged 2×3 pile group. It is observed that the lateral displacement of the pile cap slightly decreased during the vertical loading phase until the peak vertical force was reached. After reaching the peak resistance and maintaining it for approximately 1 mm of vertical displacement increment (Figure 13a), the vertical resistance of specimen #1 suddenly dropped. As shown in Figure 14(a)-1, the pile heads of the three piles on the south side of the specimen failed in shear, whereas the three piles in the north side of the specimen exhibited a flexural failure mode, which was induced by the cap tilt along the north-south direction.

The residual vertical load-carrying capacity of specimen #2 was 882 kN, which corresponded to 52.5% of the initial vertical load-carrying capacity of the pile group. It is observed that the cap lateral displacement for this specimen remained almost constant until the peak vertical resistance was reached at approximately 4.3 mm. After the peak vertical strength was reached, the lateral displacement of the cap started increasing significantly until the specimen suddenly failed in flexure (see Figure 14(b)-1), with the cap rotating vertically about the north-south axis (Figure 14(b)-2) and twisting about the vertical axis (Figure 14(b)-3). The twisting of the cap is highlighted by the non-parallel traces of the container wall and the cap edge, which are shown by dashed red lines in Figure 14(b)-3.

The residual vertical load-carrying capacity of specimen #3 was 440 kN, which corresponded to 26.2% of the initial vertical load-carrying capacity of the pile group. Figure 14(c) shows some pictures of the post-test conditions of the physical specimen. This specimen failed following a flexural failure mode with a pronounced rotation of the cap in the north-south direction. As shown in Figure 13(b), the cap lateral displacement gradually increased from the initial residual displacement for increasing vertical displacement.

As shown in Figure 14(c)-2, the confinement effect provided by the sand inhibited the spalling of cover concrete in the plastic hinge regions of the belowground pile shafts, even after the pile shaft suffered severe flexural damage. For specimens #2 and #3, the flexural deformation gradually decreased from the piles in the first row to those in the third row with respect to the direction of the cap residual displacement. The embedded depth of the plastic hinge centers on the belowground pile shafts were approximately 4D, 5D, and 6D in sequence, which corresponded to shallower depths than those obtained from curvature measurements during the cyclic loading phases of the test and reported in Figure 8. This phenomenon was observed because specimens #2 and #3 experienced relatively large lateral displacements (i.e., more than 12 cm) induced by the vertical loads applied during the pushdown phase, and the embedded depth of the belowground plastic hinge in each pile tended to decrease for increasing lateral displacement levels. It is noteworthy that no cracks were observed on the piles at a depth higher than 14D from the soil surface. Finally, by using a plumb bob hung from the bottom of the cap (see Figures 14(a)-3 and 14(c)-3), it was observed that the belowground portions of the pile shafts remained almost vertical and undamaged in specimen #1, whereas they remained practically vertical and undamaged below the belowground plastic hinges in specimens #2 and #3. Therefore, it is concluded that the pile damage induced by lateral loads were mainly concentrated in the pile heads and in the upper portions embedded in the sand (i.e., between 3D and 10D below the soil surface) for the scoured pile groups. This pile damage led to a permanent displacement and tilt on the cap, and dominated the residual vertical load capacity and the vertical failure mode of the pile group foundations.

Vertical load-carrying capacity degradation

The test results demonstrated that the pile damage after the cyclic loading phases affected significantly the residual vertical load-carrying capacity of the pile groups and their failure modes induced by vertical loads. Figure 15 illustrates the experimentally-derived vertical load-carrying capacity degradation (expressed as vertical peak strength normalized by the estimated peak strength of the undamaged pile group) as a function of the peak displacement ductility of the pile groups. The data points obtained from the pushdown tests were fitted by using a piecewise linear function given by:

$$\frac{P_R}{P_0} = \begin{cases} 1 & 0 \le \mu_D \le 1 \\ 1.185 - 0.185\mu_D & 1 < \mu_D \le 5 \end{cases} \tag{4}$$

where P_R and P_0 denote the residual and initial vertical load-carrying capacity of the pile group, respectively. This proposed equation is based on two assumptions: (1) no losses in the vertical load-carrying capacity of the pile groups are suffered if the displacement ductility is less than or equal to 1.0; and (2) the degradation of the vertical load-carrying capacity is assumed linear in the range $1.0 \leq \mu_D \leq 5.0$. The high value of the coefficient of determination $R^2 = 0.996$ suggests that the linear model proposed in this study is appropriate. It is noteworthy that Equation 4 is valid only for the specific conditions representing the experimental tests reported in this paper. However, the proposed vertical load-carrying capacity degradation curve could represents a starting point to develop more general curves to predict the residual vertical load-carrying capacity of damaged scoured pile groups, e.g., for bridge rating and post-earthquake rapid assessment applications. However, in order to develop such curves, additional experimental results are needed considering, at a minimum: different pile configurations, sizes, and numbers; different material properties; different scour depths; and different soil profiles and conditions.

Conclusions

This study investigated the seismic failure mechanism and post-earthquake vertical load-carrying capacity of scoured pile group foundations. Three identical 2×3 pile group specimens were embedded in homogeneous sand, compacted to a relative density D_r = 51-58% with an overall scour depth of 5D, where D = 12 cm denotes the diameter of a single pile. The soil container had dimensions of 310 cm and 150 cm in the directions parallel and perpendicular to the cyclic loading direction. This configuration allowed a distance of all piles of at least 113 cm (9.42D) and 51 cm (4.25D) from the soil container boundary in the directions parallel and perpendicular to the cyclic loading direction. It was shown that these distances were sufficient to render almost negligible the boundary effects on the pile-soil interaction. The three specimens were first subjected to a horizontal cyclic loading applied to pile cap to simulate the effects of earthquake loads. The maximum intensity of the cyclic loading was selected to produce three different predetermined damage states. The damaged pile group specimens (i.e., with a residual lateral displacement) were then subjected to a pushdown test to evaluate their residual load-carrying capacity. This study produced the following main findings:

(1) For the considered scoured pile group, the piles aligned along the lateral load direction formed a frame-like structure due to the constraints imposed by surrounding soil and the pile-cap connection. Each pile in the pile group exhibited two potential plastic hinge locations: the first one was located at the pile head, and the second one was located in the belowground portion of the pile shaft. Both the first aboveground and first belowground plastic hinges occurred on the leading piles when the scoured pile groups were subjected to the cyclic loading representing the earthquake loading effects. Thus, the test results presented in this study suggest that the leading

piles are more prone to seismic damage than internal piles in pile group foundations. In addition, the embedded depth of the belowground plastic hinges gradually increased from leading, to middle, and to trailing piles. For a given pile, the embedded depth of the belowground plastic hinge decreased for increasing lateral displacement levels.

(2) The three pile group specimens experienced a degradation of their vertical load-carrying capacity of 10.4%, 47.5%, and 73.8%, corresponding to a peak displacement ductility of 1.75, 3.5 and 5.0, respectively. The failure mode under vertical loading changed for different residual cap lateral displacements, with a shear failure for specimen #1 (corresponding to a peak displacement ductility of 1.75), a mixed flexural-torsional failure for specimen #2 (corresponding to a peak displacement ductility of 3.5), and a flexural failure for specimen #3 (corresponding to a peak displacement ductility of 5.0).

(3) The damage induced on the piles by the cyclic loading resulted in a linear degradation of the residual vertical load-carrying capacity of the pile groups. In particular, the residual vertical load-carrying capacity of the pile group specimens decreased linearly for increasing peak displacement ductility larger than 1.0. A piecewise linear function was fitted to the experimental results.

It is noteworthy that this paper focuses mainly on the seismic failure mechanism and the residual vertical load-carrying capacity of 2×3 scoured pile groups in a homogeneous sand for different damage levels induced by cyclic loading and expressed in terms of peak cap displacement ductility. The configuration of the experiment is representative of a pile group with end bearing on rock/stiff substrata. The experimental results presented in this study could be used to validate three-dimensional nonlinear finite-element models for evaluating the peak ductility capacity and the residual vertical load-carrying capacity of scoured pile groups damaged by earthquakes under different conditions than those used in the experiments reported here. Further studies are needed to quantify the impacts of different soil conditions and profiles, pile layouts, material properties, and scour depths on the residual vertical load-carrying capacity of scoured pile groups damaged by earthquakes.

Data Availability Statement

Some or all data, models, or code that support the findings of this study (including the section analysis executable codes and the force-displacement data for the pile group specimens) are available from the corresponding author upon reasonable request.

Acknowledgements

The authors gratefully acknowledge the funding support of this work by the National Natural Science Foundation of China (Grant No. 51778469). The first author is thankful for the financial support from the China Scholarship Council. Any opinions, findings, and conclusions expressed are those of the authors, and do not necessarily reflect those of the sponsoring organizations. All staff members in the Multi-Functional Shaking Table Laboratory of Tongji University at Jiading Campus are also gratefully acknowledged.

References

ACI (American Concrete Institute). 2014. *Building code requirements for structural concrete*. ACI 318-14, Farmington Hills, MI: ACI.

Banerjee, S., Stanton, J. F., and Hawkins, N. M. 1987. “Seismic performance of precast prestressed concrete piles.” *J. Struc. Eng.* 113(2), 381–396. https://doi.org/10.1061/(ASCE)0733-9445(1987)113:2(381).

Barbato, M., Gu, Q., and Conte, J. P. 2010. “Probabilistic push-over analysis of structural and soil-structure systems.” *J. Struc. Eng.* 136(11), 1330–1341. https://doi.org/10.1061/(ASCE)ST.1943-541X.0000231.

Bhattacharya, S., Blakeborough, A., and Dash, S. 2008. “Learning from collapse of piles in liquefiable soils.” *Proc. Inst. Civ. Eng. - Civ. Eng.* 161(6), 54–60. https://doi.org/10.1680/cien.2008.161.6.54.

Blanco, G., Ye, A., Wang, X., and Goicolea, J. M. 2019. “Parametric pushover analysis on elevated RC pile-cap foundations for bridges in cohesionless soils.” *J. Bridg. Eng.* 24(1), 04018104. https://doi.org/10.1061/(ASCE)BE.1943-5592.0001328.

Chai, Y. H., and Hutchinson, T. C. 2002. “Flexural strength and ductility of extended pile-shafts II: experimental study.” *J. Struc. Eng.* 128(5), 595–602. https://doi.org/10.1061/(ASCE)0733-9445(2002)128:5(595).

Elwood, K. J., and Moehle, J. P. 2005. “Axial capacity model for shear-damaged columns.” *ACI Struct. J.* 102(4), 1–37. https://doi:10.14359/14562.

Filippou, F. C., Popov, E. P., and Bertero, V. V. 1983. *Effects of bond deterioration on hysteretic behaviour of reinforced concrete joints*. Earthquake Engineering Research Center,University of California, Berkeley.

Guan, Z., Zhang, J., and Li, J. 2017. “Multilevel performance classifications of tall RC bridge columns toward postearthquake rehabilitation requirements." *J. Bridg. Eng.* 22(10), 04017080. https://doi.org/10.1061/(ASCE)BE.1943-5592.0001111.

Hose, Y. D., and Seible, F. 1999. *Performance evaluation database for concrete bridge components and systems under simulated seismic loads*. Pacific Earthquake Research Center, PEER 11, Berkeley, CA.

Kawashima, K., Takahashi, Y., Ge, H., Wu, Z., and Zhang, J. 2009. "Reconnaissance report on damage of bridges in 2008 Wenchuan, China, earthquake." *J. Earthq. Eng.* 13(7), 965–996. https://doi.org/10.1080/13632460902859169.

Lam, S. S. E., Wu, B., Wong, Y. L., Wang, Z. Y., Liu, Z. Q., and Li, C. S. 2003. "Drift capacity of rectangular reinforced concrete columns with low lateral confinement and high-axial load." *J. Struc. Eng.* 129(6), 733–742. https://doi.org/10.1061/(ASCE)0733-9445(2003)129:6(733).

Lemnitzer, A., Khalili-Tehrani, P., Ahlberg, E. R., Rha, C., Taciroglu, E., Wallace, J. W., and Stewart, J. P. 2010. "Nonlinear efficiency of bored pile group under lateral loading." *J. Geotech. Geoenvironmental Eng.* 136(12), 1673–1685. https://doi.org/10.1061/(ASCE)GT.1943-5606.0000383.

Lin, S.-S., and Liao, J.-C. 1999. "Permanent strains of piles in sand due to cyclic lateral loads." *J. Geotech. Geoenvironmental Eng*. 125(9), 798–802. https://doi.org/10.1061/(ASCE)1090-0241(1999)125:9(798).

Liu, T., Wang, X., and Ye, A. 2020. "Roles of pile group and cap-rotation effects on seismic failure mechanisms of partially-embedded bridge foundations: Quasi-static tests." *Soil Dyn. Earthq. Eng*. 132, 106074. https://doi.org/10.1016/j.soildyn.2020.106074.

Mander J.B., Dutta A., and Goel P. 1998. *Capacity design of bridge piers and the analysis of overstrength*. MCEER-98-0003.

Mazzoni, S., McKenna, F., Scott, M. H., and Fenves, G. L. 2006. *OpenSees command language manual*. Pacific Earthquake Engineering Research Center, Berkeley, CA.

McKenna, F. 2011. "OpenSees: A framework for earthquake engineering simulation." *Comput. Sci. Eng.* 13(4), 58–66. https://doi.10.1109/MCSE.2011.66.

O'Connor, J., and Alampalli, S. 2010. "Post-earthquake bridge inspection guide lines for NewYork state." *Bridg. Maintenance, Safety, Manag. Life-Cycle Optim. - Proc. 5th Int. Conf. Bridg. Maintenance, Saf. Manag*. 160–160.

Park, R., and Falconer, T. J. 1983. "Ductility of prestressed concrete piles subjected to simulated seismic loading." *PCI J.*

28(5), 112–144. https://doi:10.15554/pcij.09011983.112.144.

Rollins, K. M., Johnson, S. R., Petersen, K. T., and Weaver, T. J. 2003. "Static and dynamic lateral load behavior of pile groups based on full-scale testing." *Proc. Int. Offshore Polar Eng. Conf.,* International Society of Offshore and Polar Engineers.

Rollins, K. M., Lane, J. D., and Gerber, T. M. 2005. "Measured and computed lateral response of a pile group in sand." *J. Geotech. Geoenvironmental Eng.* 131(1), 103–114. https://doi.org/10.1061/(ASCE)1090-0241(2005)131:1(103).

Rollins, K. M., Olsen, K. G., Jensen, D. H., Garrett, B. H., Olsen, R. J., and Egbert, J. J. 2006. "Pile spacing effects on lateral pile group behavior: analysis." *J. Geotech. Geoenvironmental Eng.* 132(10), 1272–1283. https://doi.org/10.1061/(ASCE)1090-0241(2006)132:10(1272).

Scott, B. D., Park, R., and Priestley, M. J. N. 1982. "Stress-strain behavior of concrete confined by overlapping hoops at low and high strain rates." *ACI J. Proc.* 79(1), 13–27. https://doi:10.14359/10875.

Shang, Y., Alipour, A., and Ye, A. 2018. "Selection of input motion for seismic analysis of scoured pile-supported bridge with simplified models." *J. Struc. Eng.* 144(8), 04018099. https://doi.org/10.1061/(ASCE)ST.1943-541X.0002067.

Tasai, A. 2000. *Residual axial capacity of reinforced concrete columns during shear degradation.* Pacific Earthquake Engineering Research Center, PEER 10, Berkeley, CA, 257-267.

Terzic, V., and Stojadinovic, B. 2015a. "Evaluation of post-earthquake axial load capacity of circular bridge columns." *ACI Struct. J*. 112(1), 23–34. https://doi: 10.14359/51687296.

Terzic, V., and Stojadinovic, B. 2015b. "Calibration and validation of analytical models for predicting the seismic and axial-load response of circular bridge columns." *J. Bridg. Eng.* 20(9), 04014098. https://doi.org/10.1061/(ASCE)BE.1943-5592.0000702.

Wang, S.-C., Liu, K.-Y., Chen, C.-H., and Chang, K.-C. 2015. "Experimental investigation on seismic behavior of scoured bridge pier with pile foundation." *Earthq. Eng. Struct. Dyn.* 44(6), 849–864. https://doi.org/10.1002/eqe.2489.

Wang, X., Fang, J., Zhou, L., and Ye, A. 2019a. "Transverse seismic failure mechanism and ductility of reinforced concrete pylon for long span cable-stayed bridges: Model test and numerical analysis." *Eng. Struc.* 189, 206–221. https://doi.org/10.1016/j.engstruct.2019.03.045.

Wang, X., Shafieezadeh, A., and Ye, A. 2019b. “Optimal EDPs for post-earthquake damage assessment of extended pile-shaft–supported bridges subjected to transverse spreading.” *Earthq. Spectra,* 35(3), 1367–1396. https://doi.org/10.1193/090417EQS171M.

Wang, X., Ye, A., He, Z., and Shang, Y. 2016. “Quasi-static cyclic testing of elevated rc pile-cap foundation for bridge structures.” *J. Bridg. Eng.* 21(2), 04015042. https://doi.org/10.1061/(ASCE)BE.1943-5592.0000797.

Wang, X., Ye, A., and Ji, B. 2019c. “Fragility-based sensitivity analysis on the seismic performance of pile-group-supported bridges in liquefiable ground undergoing scour potentials.” *Eng. Struc.* 198, 109427. https://doi.org/10.1016/j.engstruct.2019.109427.

Wang, X., Ye, A., Shang, Y., and Zhou, L. 2019d. “Shake-table investigation of scoured RC pile-group-supported bridges in liquefiable and nonliquefiable soils.” *Earthq. Eng. Struct. Dyn.* 48(11), 1217–1237. https://doi.org/10.1002/eqe.3186.

Wang, Z., Dueñas-Osorio, L., and Padgett, J. E. 2014. “Influence of scour effects on the seismic response of reinforced concrete bridges.” *Eng. Struc.* 76, 202–214. https://doi.org/10.1016/j.engstruct.2014.06.026.

Wardhana, K., and Hadipriono, F. C. 2003. “Analysis of recent bridge failures in the united states.” *J. Perform. Constr. Facil.* 17(3), 144–150. https://doi.org/10.1061/(ASCE)0887-3828(2003)17:3(144).

Wei, X., Wang, Q., and Wang, J. 2008. “Damage patterns and failure mechanisms of bridge pile foundation under earthquake.” *14th World Conf. Earthq. Eng.*, Beijing, China.

Yeh, Y.-K., Mo, Y. L., and Yang, C. Y. 2002. “Seismic performance of rectangular hollow bridge columns.” *J. Struc. Eng.* 128(1), 60–68. https://doi.org/10.1061/(ASCE)0733-9445(2002)128:1(60).

Zhou, L., Wang, X., and Ye, A. 2019. “Shake table test on transverse steel damper seismic system for long span cable-stayed bridges.” *Eng. Struc.* 179, 106–119. https://doi.org/10.1016/j.engstruct.2018.10.073.

Tables

Table 1. Mechanical properties of concrete and steel reinforcements

Material	Elastic modulus (MPa)	Yield strength (MPa)	Peak strength (MPa)	Strain corresponding to peak strength
Concrete	32260 (3.2%)	--	25.2 (1.6%)	--
ϕ6mm rebars	216353 (5.1%)	429 (3.7%)	670 (3.2%)	0.120 (2.1%)
ϕ3.5mm GIW	135441 (6.3%)	317 (4.0%)	421 (2.2%)	0.148 (11.2%)

Note: data in the parentheses refer to the variation coefficient.

Table 2. Test matrix

Specimen	Lateral damage state target	Peak lateral disp./mm	Test sequences
#1	First yielding of belowground pile shaft	35	Lateral and vertical
#2	Onset of lateral strength degradation (or peak strength)	70	Lateral and vertical
#3	15% lateral strength degradation	100	Lateral and vertical

Table 3. Pile head curvatures calculated through the data from linear potentiometers

Loading direction	Disp. level (mm)	Curvatures (rad/m)		
		Pile 1	Middle pile	Pile 3
Push	+35	-0.196	-0.103	-0.150
	+70	-0.570	-0.398	-0.319
	+100	-0.923	-0.604	-0.449
Pull	-35	0.134	0.142	0.247
	-70	0.362	0.379	0.498
	-100	0.556	0.666	0.825

Table 4. Peak displacement and curvature ductility of the test specimens

Specimen	Lateral damage state	Displacement ductility	Maximum curvature ductility of first aboveground plastic hinge
#1	First belowground yielding of pile shaft	1.75	5.49
#2	Onset of lateral strength degradation	3.50	12.67
#3	15% lateral strength degradation	5.00	20.51

Table 5. Global performance and local damage descriptions for the pile group specimens

Specimen	Performance description	Peak displacement ductility	Residual cap displacement (mm)	Residual cap rotation (rad$\times 10^{-3}$)	Residual crack width (mm)	Observed aboveground pile damage description
#1	First belowground yielding	1.75	14	0.0	0.28	Hairline residual cracks near pile head regions
#2	Onset of lateral strength degradation	3.50	40	0.7	0.98	Slight concrete spalling at pile head
#3	15% lateral strength degradation	5.00	68	3.9	--	Extensive cover concrete spalling and local core concrete crushing

Note: The residual crack width was measured on the leading pile at the west side of the specimens at approximately 8 cm below the pile head.

Figure captions

Figure 1. Quasi-static test overview and instrumentations: (a) side view of schematic diagram, (b) plan view of schematic diagram, (c) pile reinforcement and strain gage distribution over a single pile, and (d) single pile cross-section (all units are in cm if not otherwise indicated)

Figure 2. Photographs of physical test layout: (a) full-view, (b) actuator-cap connections, (c) sand and aboveground piles, (d) laser sensor positions, and (e) inclinometer

Figure 3. Numerical moment-curvature response of a pile cross-section subjected to an axial load ratio of 5%

Figure 4. Particle size distribution of test sand

Figure 5. Loading protocols

Figure 6. Comparison of soil pressures on leading pile and container walls

Figure 7. Lateral hysteretic behavior of specimens: (a) force versus displacement curves, and (b) envelope curves

Figure 8. Curvature distributions of piles at positive (push) and negative (pull) peak displacements for different loading cycles

Figure 9. Cap rotation angle: (a) versus peak lateral displacement (pull and push directions), and (b) versus displacement ductility (only positive quadrant)

Figure 10. Variations of crack width at the leading pile head: (a) hysteretic lateral force versus crack width curves, and (b) comparison of crack width at different loading states

Figure 11. Observed physical damage of the pile group specimens at the end of the corresponding lateral loading (or residual deformation state): (a) specimen #1, (b) specimen #2, and (c) specimen #3

Figure 12. Axial force-strain curves for the short columns

Figure 13. Residual vertical load-carrying capacity of pile group foundations under different damage levels: (a) vertical load versus vertical displacement increment, and (b) lateral displacement versus vertical displacement increment

Figure 14. Post-test observations of the physical specimens after soil removal: (a) specimen #1, (b) specimen #2, and (c) specimen #3

Figure 15. Vertical load capacity degradation data and fitting curve

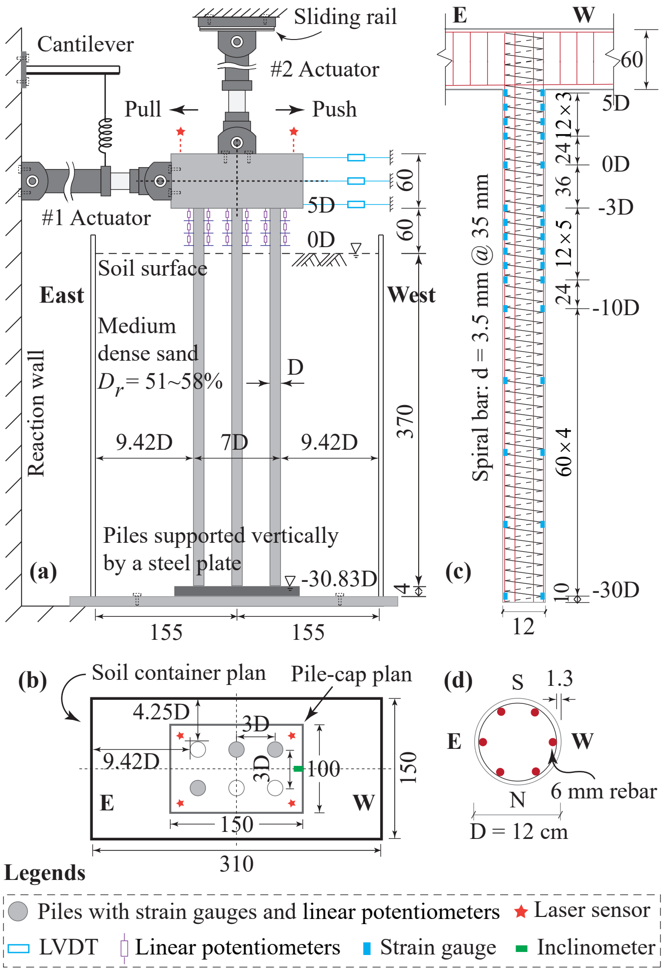

Sliding rail
Cantilever
#2 Actuator
Pull
Push
#1 Actuator
5D
0D
60
60
Soil surface
East
West
Medium
dense sand
D_r = 51~58%
D
Reaction wall
9.42D
7D
9.42D
370
Piles supported vertically
by a steel plate
(a)
-30.83D
4
155
155
E
W
60
5D
0D
-3D
-10D
-30D
12×3
24
36
12×5
24
60×4
10
12
Spiral bar: d = 3.5 mm @ 35 mm
(c)
(b)
Soil container plan
Pile-cap plan
4.25D
3D
9.42D
3D
100
150
E
W
150
310
(d)
S
1.3
E
W
N
6 mm rebar
D = 12 cm
Legends
Piles with strain gauges and linear potentiometers
Laser sensor
LVDT
Linear potentiometers
Strain gauge
Inclinometer

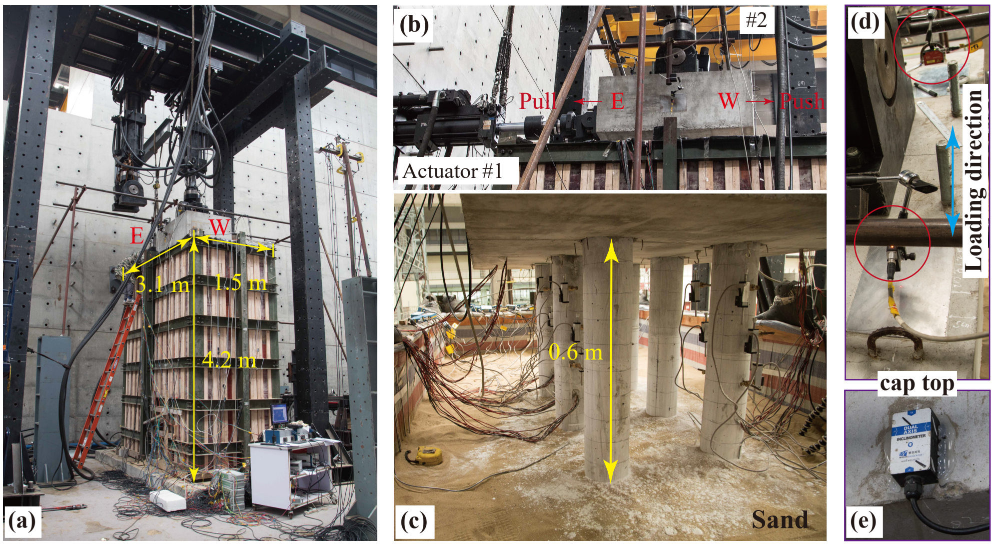

E
W
3.1 m
1.5 m
4.2 m
(a)
(b)
#2
Pull
E
W
Push
Actuator #1
(c)
0.6 m
Sand
(d)
Loading direction
cap top
(e)

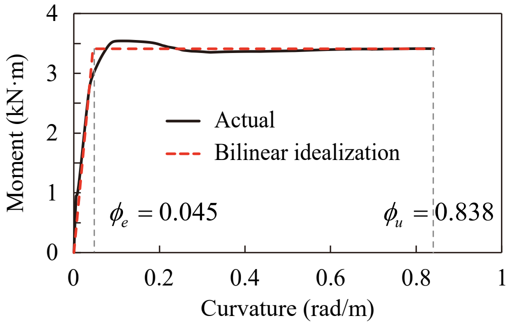

Moment (kN·m)
Curvature (rad/m)
0
1
2
3
4
0.2
0.4
0.6
0.8
Actual
Bilinear idealization
$\phi_e = 0.045$
$\phi_u = 0.838$

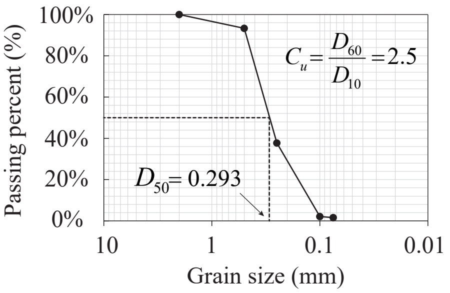
100%
80%
60%
40%
20%
0%
Passing percent (%)
$C_u = \frac{D_{60}}{D_{10}} = 2.5$
$D_{50} = 0.293$
10
1
0.1
0.01
Grain size (mm)

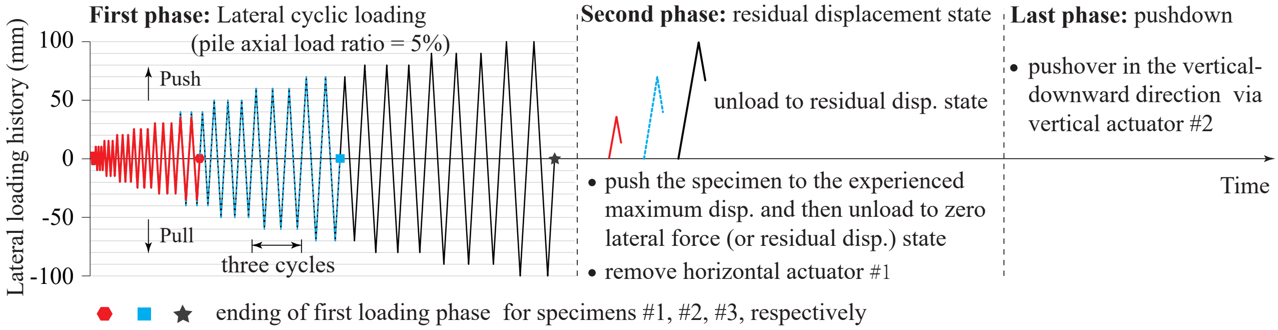

First phase: Lateral cyclic loading
(pile axial load ratio = 5%)
Second phase: residual displacement state
Last phase: pushdown
Lateral loading history (mm)
100
50
0
-50
-100
Push
Pull
three cycles
unload to residual disp. state
• push the specimen to the experienced maximum disp. and then unload to zero lateral force (or residual disp.) state
• remove horizontal actuator #1
• pushover in the vertical-downward direction via vertical actuator #2
Time
ending of first loading phase for specimens #1, #2, #3, respectively

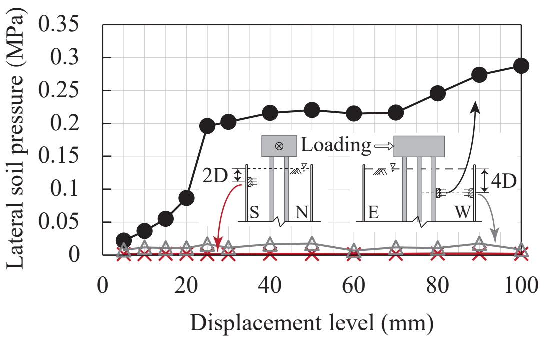

Lateral soil pressure (MPa)
0.35
0.3
0.25
0.2
0.15
0.1
0.05
0
0
20
40
60
80
100
Displacement level (mm)
Loading
2D
4D
S
N
E
W

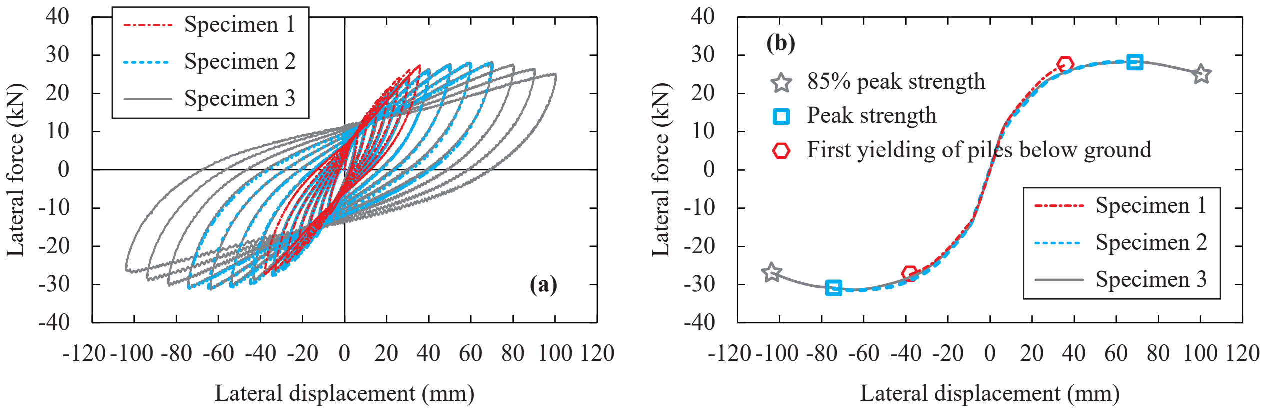

Specimen 1
Specimen 2
Specimen 3
(a)
Lateral force (kN)
Lateral displacement (mm)
40
30
20
10
0
-10
-20
-30
-40
-120 -100 -80 -60 -40 -20 0 20 40 60 80 100 120
(b)
85% peak strength
Peak strength
First yielding of piles below ground
Specimen 1
Specimen 2
Specimen 3
Lateral force (kN)
Lateral displacement (mm)

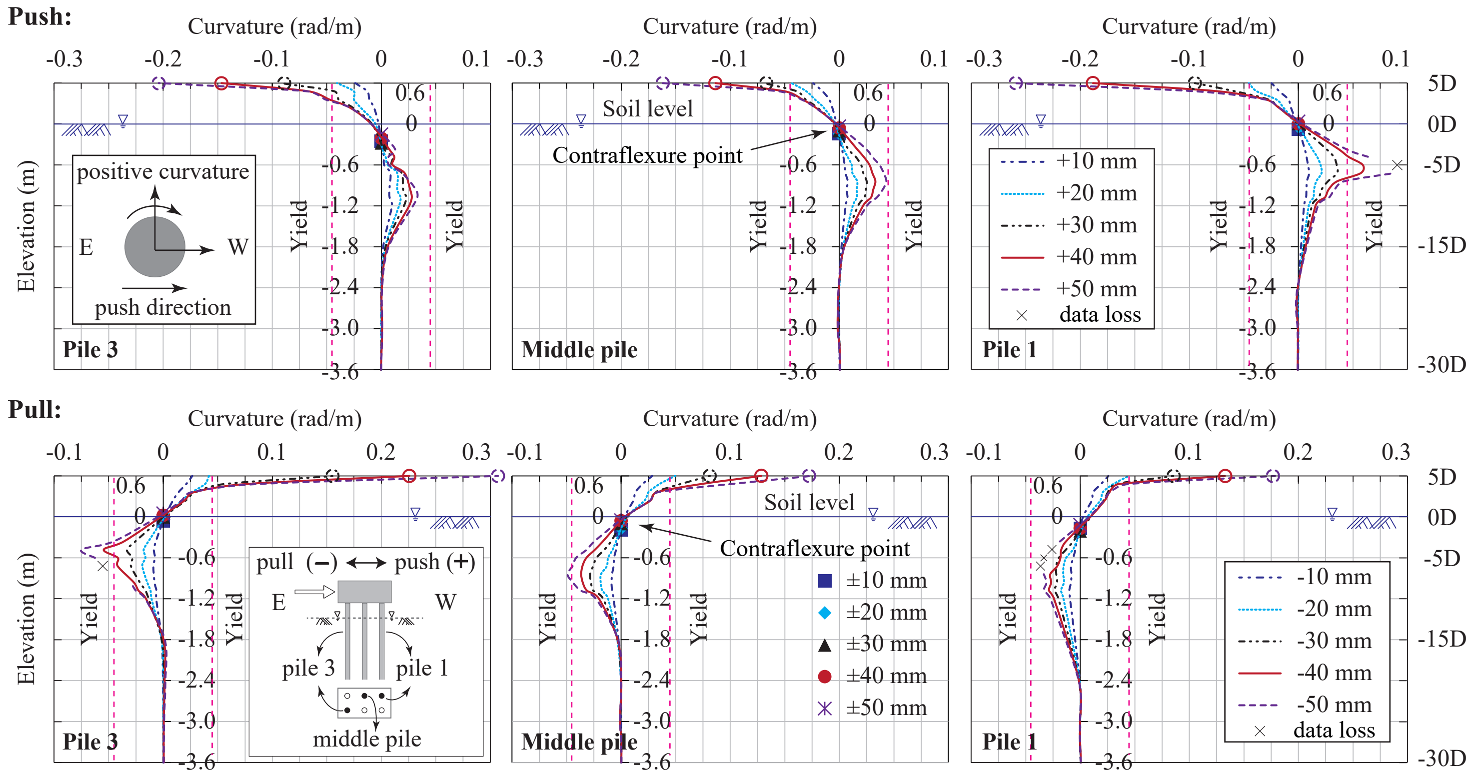

Push:
Curvature (rad/m)
Elevation (m)
positive curvature
E
W
push direction
Yield
Soil level
Contraflexure point
Pile 3
Middle pile
Pile 1
+10 mm
+20 mm
+30 mm
+40 mm
+50 mm
data loss
5D
0D
-5D
-15D
-30D
Pull:
pull (−) ↔ push (+)
pile 3
pile 1
middle pile
±10 mm
±20 mm
±30 mm
±40 mm
±50 mm
-10 mm
-20 mm
-30 mm
-40 mm
-50 mm

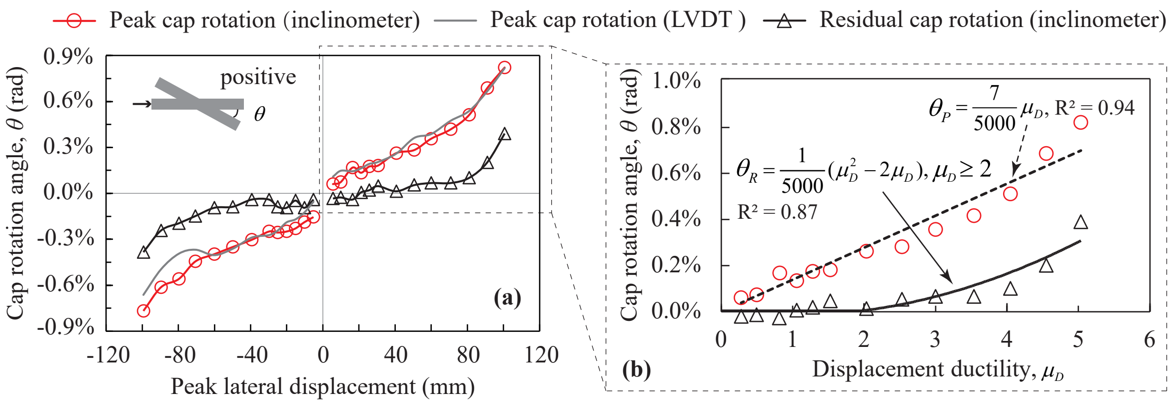

Peak cap rotation (inclinometer)
Peak cap rotation (LVDT)
Residual cap rotation (inclinometer)
Cap rotation angle, θ (rad)
positive
θ
(a)
Peak lateral displacement (mm)
0.9%
0.6%
0.3%
0.0%
-0.3%
-0.6%
-0.9%
-120
-80
-40
0
40
80
120
Cap rotation angle, θ (rad)
1.0%
0.8%
0.6%
0.4%
0.2%
0.0%
$\theta_P = \frac{7}{5000}\mu_D$, R² = 0.94
$\theta_R = \frac{1}{5000}(\mu_D^2 - 2\mu_D)$, $\mu_D \geq 2$
R² = 0.87
(b)
Displacement ductility, μ_D
0
1
2
3
4
5
6

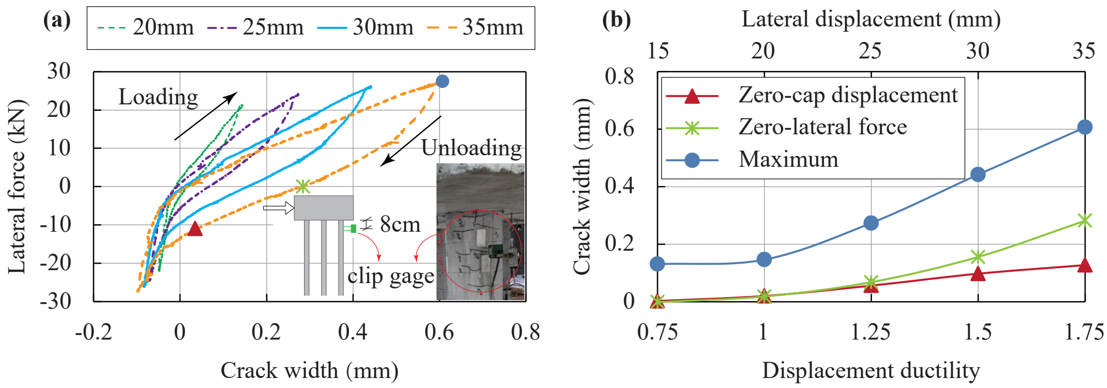
(a)
20mm
25mm
30mm
35mm
Loading
Unloading
8cm
clip gage
Lateral force (kN)
Crack width (mm)
30
20
10
0
-10
-20
-30
-0.2
0
0.2
0.4
0.6
0.8
(b)
Lateral displacement (mm)
15
20
25
30
35
Zero-cap displacement
Zero-lateral force
Maximum
Crack width (mm)
0.8
0.6
0.4
0.2
0
0.75
1
1.25
1.5
1.75
Displacement ductility

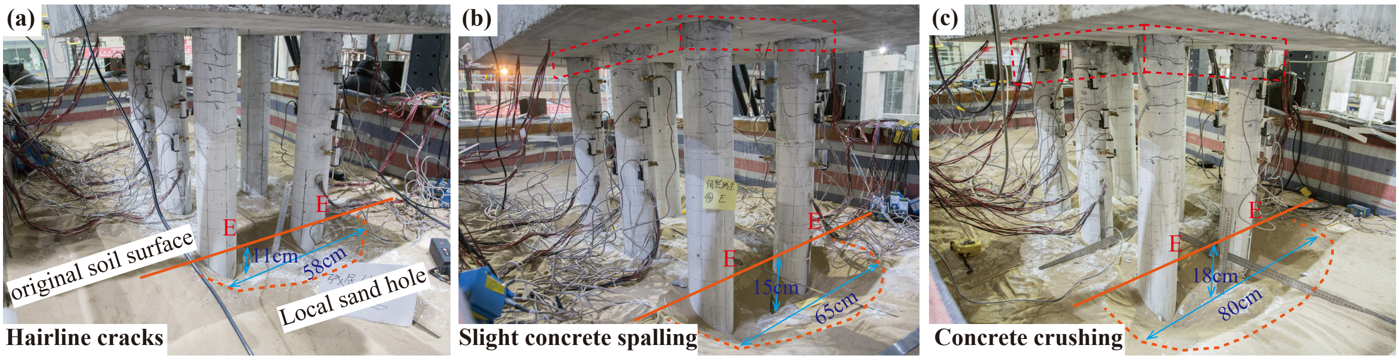
(a)
original soil surface
E
E
11cm
58cm
Local sand hole
Hairline cracks
(b)
E
E
15cm
65cm
Slight concrete spalling
(c)
E
E
18cm
80cm
Concrete crushing

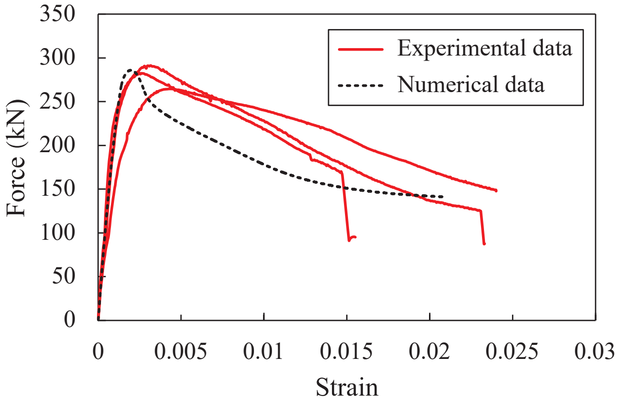

Force (kN)
350
300
250
200
150
100
50
0
0
0.005
0.01
0.015
0.02
0.025
0.03
Strain
Experimental data
Numerical data

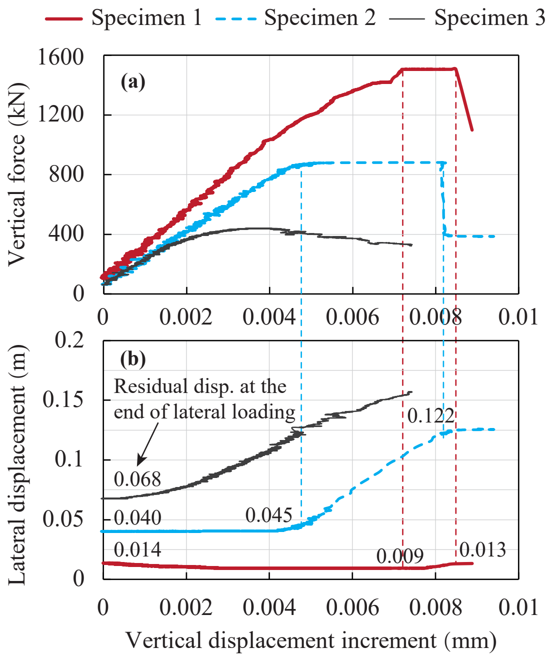

Specimen 1
Specimen 2
Specimen 3
(a)
Vertical force (kN)
1600
1200
800
400
0
0
0.002
0.004
0.006
0.008
0.01
(b)
Residual disp. at the end of lateral loading
0.068
0.040
0.045
0.014
0.009
0.013
0.122
Lateral displacement (m)
0.2
0.15
0.1
0.05
0
Vertical displacement increment (mm)

W
N
S
E
(a)-1
W
(a)-2
W
E
Plumb bob
(a)-3
W
N
S
E
(b)-1
W
(b)-2
W
E
(b)-3
W
N
S
E
(c)-1
W
original soil surface
5D
4D
(c)-2
E
W
Plumb bob
(c)-3

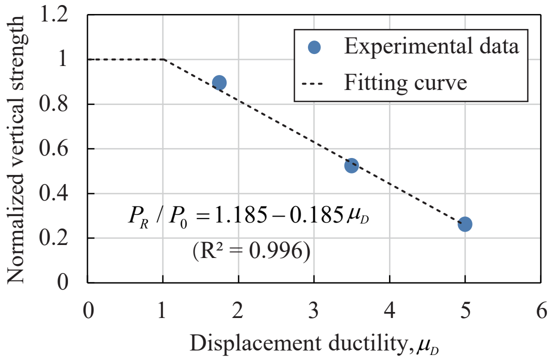

Normalized vertical strength
1.2
1
0.8
0.6
0.4
0.2
0
0
1
2
3
4
5
6
Displacement ductility, μ_D
Experimental data
Fitting curve
$P_R / P_0 = 1.185 - 0.185\mu_D$
($R^2 = 0.996$)